Acoustic wave focusing by doubly curved origami-inspired arrays

Vivek Srinivas and Ryan L Harne(iD)

Abstract

Spherically focused transducers have been long relied on to target acoustic energy delivery. Yet, these structures have limitations with respect to size and mobility for medical treatment applications. Recent developments in the field of reconfigurable structures reveal that the ancient art of origami inspires new platforms by which to enable spherical shapes that are additionally foldable for ease of transport. This research explores the opportunities for a unique, flat foldable doubly curved tessellated array to enable wave focusing capability similar to an ideal medical transducer shape: the spherical cap transducer. An analytical model of the doubly curved array is created and validated against data collected from a proof-of-concept array. The model is then leveraged to understand how the array design and complexity relatively govern the wave focusing capability. The findings show that doubly curved acoustic arrays do not require excessive facet refinement to achieve wave focusing similar to nominal spherically focused transducers. Yet, the optimal frequencies for which such capability is borne out vary substantially on the basis of array design. The discoveries of this research motivate future consideration of flat foldable doubly curved acoustic arrays for potential implementation into medical transducer development for hard-to-access surgical treatments.

Keywords

Doubly curved, foldable, focusing, acoustics, origami, sound radiation, ultrasound, tumor ablation, spherically focused transducer

1. Introduction

Wave focusing properties of spherically focused transducers are employed in various areas of engineering and medical fields. Numerous applications of these transducers are found in optics (Li et al., 1985), underwater communication (Merkens and Oleson, 2018), structural health monitoring (Koduru and Rose, 2012), ultrasound-based surgery (Ji et al., 2008), medical imaging (Cantinotti et al., 2018; Vilkomerson et al., 1992), radiology (Kennedy, 2005; Wu and Sherar, 2002), and more. These focusing transducers take on one of two surface profiles: the spherical segment is the shape defined by cutting a sphere with a pair of parallel planes, whereas a spherical cap is the smaller part of a sphere cut by a single plane. High-intensity focused ultrasound (HIFU) (Kennedy, 2005) is one such technique where such spherically focused transducers are used to focus ultrasonic waves. HIFU transducers excite surface-mounted piezoelectric material to radiate ultrasound and focus the emitted waves at the spherical center (Aronov et al., 2012). Tumors are then destroyed by thermal ablation near the focal point (Ter Haar, 1999). Although practices of HIFU are revolutionary

as effective cancer treatment, the transducer devices are challenged to access cancers deep below the epidermis, encouraging development of versatile HIFU platforms that enable pin-point wave focusing at the diseased tumor regions.

Recent advancements for space-sensitive applications have been achieved using inspiring principles from origami science. Arrays of origami-inspired reconfigurable structures have been considered for use in space structures (Zirbel et al., 2013), antennas (Alharbi et al., 2018; Liu et al., 2015), biomedical devices (Fernandes and Gracias, 2012; Kuribayashi et al., 2006), optical platforms (Cybulski et al., 2014; Myer and Cooke, 1969), and more. These concepts are recently extended to the emerging area of reconfigurable acoustic wave guiding/focusing structures. For instance, tessellated

Department of Mechanical and Aerospace Engineering, The Ohio State University, Columbus, OH, USA

Corresponding author:
Ryan L Harne, Department of Mechanical and Aerospace Engineering, The Ohio State University, Columbus, OH 43210, USA.
Email: harne.3@osu.edu

water-bomb and star-based arrays of acoustic transducers studied by Lynd et al. (2017) and Zou et al. (2018) have wave guiding properties in the near and far field in addition to the ability to fold into compact shapes for transport. Moreover, the reconfiguration of such origami-inspired acoustic arrays empowers means to control interference phenomena and thus modulate the wave guiding properties (Lynd and Harne, 2017; Zou et al., 2018; Zou and Harne, 2017, 2018).

Miura-ori (Gattas et al., 2013; Tachi, 2009) is one of the most commonly studied tessellations for applications of origami science. Miura-ori is developable, is flat foldable using a single degree-of-freedom fold, and possesses numerous derivatives on the basis of crease pattern perturbations (Dudte et al., 2016). In addition, nearly arbitrary curvature may be introduced into Miura-ori using gradients (Dudte et al., 2016; Gattas et al., 2013). For practices of acoustic wave focusing, it is necessary to create curvature of the activated facets to radiate waves toward a common focal region (Zou et al., 2018). Song et al. (2017) studied doubly curved origami structures based on Miura-ori and adopted spherical and aspherical profiles for the curvature. The study reported the design parameter relationships governing the mechanical configuration of the rotationally symmetric geometry (Song et al., 2017). The doubly curved Miura crease pattern is of interest in the current investigation for sake of the rotationally symmetric shape created by the partially folded tessellation (Figure 1(a)), which may realize wave focusing using a design whereby the facets vibrate to produce sound. The unfolded crease pattern of a doubly curved Miura-ori is shown in Figure 1(b), revealing radial rows of unit cells and circumferential repetition of the unit cell distribution. The unit cells are identified in Figure 1(c). The crease pattern is not a continuous pattern over 2π radians around the $z-$axis because the array ends are connected in a partially folded configuration to realize the ring form shown in Figure 1(a). Yet, due to the basis on Miura-ori, the array folds flat as shown at right in Figure 1(b).

These characteristics of a tessellated acoustic array created on the doubly curved Miura-ori crease pattern encourage the following investigation. The objectives of this research are to establish an analytical model and study wave focusing functionality of doubly curved acoustic arrays. This report is organized as follows. Section 2 introduces the analytical model used to construct the array geometry and predict the radiated acoustic field from vibrating facets. Section 3 validates the model using an experimental study. Section 4 describes parametric studies on ultrasonic wave focusing capabilities enabled by small-sized doubly curved arrays that may find future application for medical

practices. Finally, the new findings are summarized with concluding discussion.

2. Model formulation

In this section, a geometric model of the doubly curved array is developed based on the relationships identified in Song et al. (2017). These geometric definitions are then used to predict acoustic pressure radiation from the vibrating facets using Rayleigh's integral (Kinsler et al., 1999; Williams, 1999).

2.1. Geometric modeling of the doubly curved acoustic array

To create a geometric model of the array, a unit cell is defined. Then, the relationship of the unit cell configuration with the other circumferential and radial unit cells in the array is established for folded tessellations.

The numbers of unit cells in circumferential and radial directions for the crease patterns are termed $m \times n$. The m is the number of unit cells in the circumferential direction, while n is the number of unit cells in the radial direction. Figure 1(c) shows a unit cell constituting nodes C_{11}, C_{12}, C_{13}, F_{13}, C_{23}, C_{22}, C_{21}, F_{11}, and F_{12}. The center point O of the array in the planar configuration Figure 1(b) is the origin for the three-dimensional folded array topology. The central axis of the array is the axis that passes through the center of array O, perpendicular to the plane of array in Figure 1(a). The spherical center of the array is S (Figure 1(e)). For the doubly curved acoustic array, the total number of vertices in the radial direction is $2n + 1$, while the number of vertices in the circumferential direction is $2m$.

The topology of the unfolded unit cell is defined by parameters that include cell lengths a_{ci}, a_{fi}, b_i; cell angles φ_c, φ_f; and the angle α_0 subtended by single facet on the array center O in the planar configuration as shown in Figure 1(c) and (d). Equations (1) to (3) relate the parameters (Song et al., 2017)

$$\varphi_c - \varphi_f = \alpha_0 \tag{1}$$

$$\frac{a_{ci}}{a_{fi}} = \frac{\sin \varphi_f}{\sin \varphi_c}, \quad i = 1, 2, 3, \ldots \tag{2}$$

$$b_i = b_1 + \frac{\sin \alpha_0}{\sin \varphi_c} \sum_{j=1}^{i-1} a_{cj}, \quad i = 2, 3, 4, \ldots \tag{3}$$

The folded states of the array are governed by the dihedral angles. Due to rotational symmetry, the dihedral angles along the collinear radial creases and along the circumferential creases are the same, as shown in Figure 1(d). Hence, the dihedral angles along the radial creases on lines ζ_f are denoted by θ_{fa}, while the dihedral
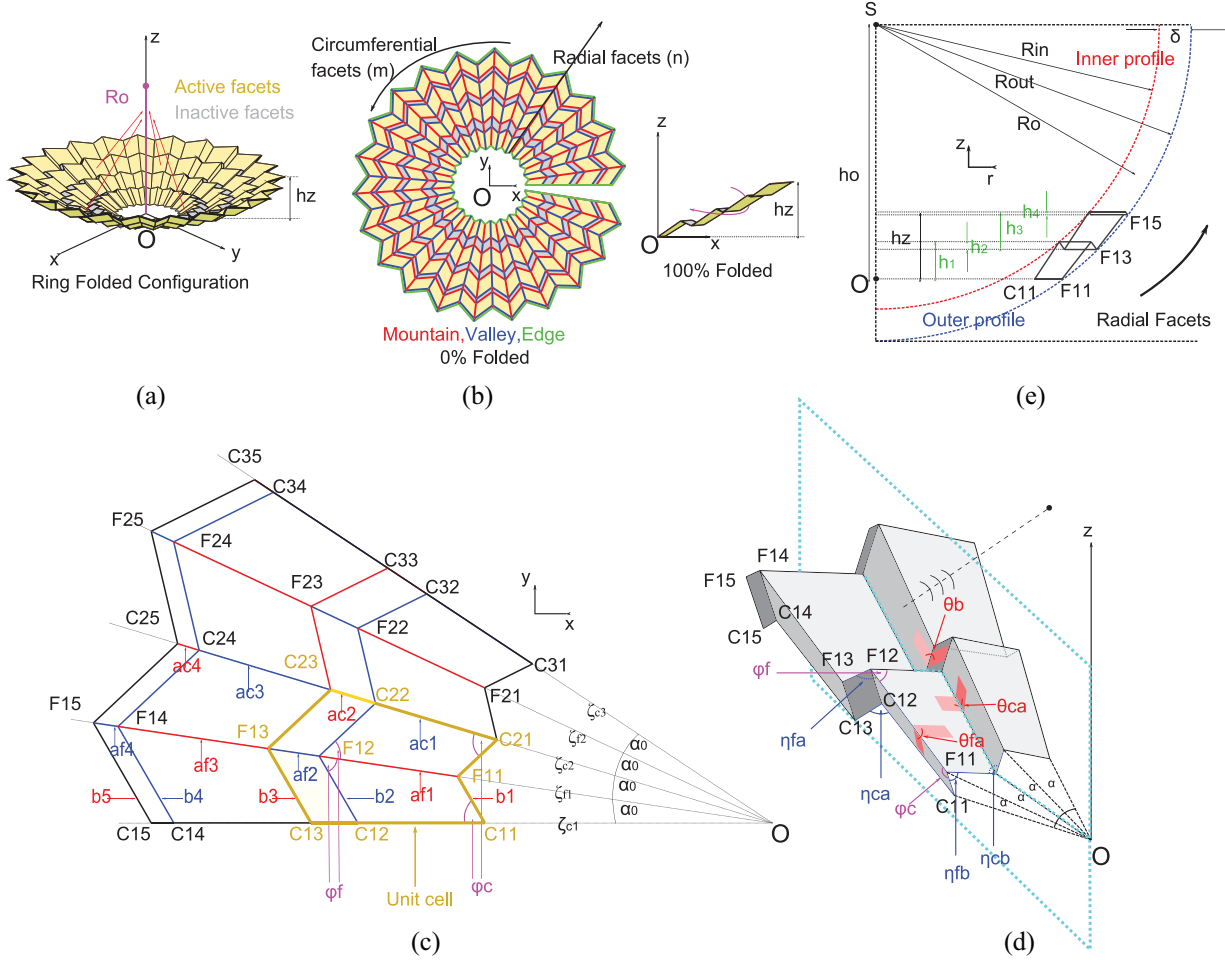
Figure 1. (a) Schematic representation of 22 × 4 array folded in a ring configuration, illustrating acoustic focusing from activated facets. R_o is the average radius of curvature of the array. (b) Crease pattern of 22 × 4 array when unfolded (at left) and when fully folded (at right). Magenta arrow indicates the direction of opening of the 100% folded array (c) Unit cell parameters and connectivity in radial and circumferential directions. (d) Partly folded view of (c). (e) Cross section showing outer and inner concentric circular profiles of (d). *O* is the array center and *S* is the spherical center.

angles along the radial creases on lines ζ_c are denoted by θ_{ca}, and those along the circumferential creases are denoted by θ_b. Equations (4) and (5) relate the dihedral angles and the cell parameters

$$\left(1 + \cos^2\varphi_c + \sin^2\varphi_c \cos\theta_{ca}\right)\left(1 + \cos^2\varphi_c - \sin^2\varphi_c \cos\theta_b\right)$$
$$= 4\cos^2\varphi_c \tag{4}$$

$$\left(1 + \cos^2\varphi_f + \sin^2\varphi_f \cos\theta_{fa}\right)\left(1 + \cos^2\varphi_f - \sin^2\varphi_f \cos\theta_b\right)$$
$$= 4\cos^2\varphi_f \tag{5}$$

There are three independent kinematic parameters θ_{fa}, θ_{ca}, and θ_b governed by equations (4) and (5). This indicates that the array has a single degree of freedom so that the folding of the array is dictated by one parameter. In this study, θ_b is chosen as the control parameter that determines the folded state of the array. For

example, in Figure 1(b), $\theta_b = 180°$ is the planar configuration, $\theta_b = 0°$ is the fully folded configuration, and in Figure 1(a) $\theta_b = 110°$ is the ring folded configuration of the array.

There are two types of vertices on the array: those vertices lying on ζ_f radial lines referred to as F-type vertices and those lying on ζ_c radial lines referred to as C-type vertices. According to Song et al. (2017), the angles formed by radial creases ζ_f and ζ_c at each internal vertices are, respectively, equal to η_{fa} and η_{ca}. Similarly, the circumferential angle counterparts are η_{fb} and η_{cb}. A single facet subtends an angle α on the array center *O*, as shown in Figure 1(d). For a given configuration θ_b, these angles have the relationship as defined in equations (6) to (10) (Song et al., 2017)

$$\cos\eta_{ca} = \sin^2\varphi_c \cos\theta_b - \cos^2\varphi_c \tag{6}$$

$$\cos\eta_{cb} = \sin^2\varphi_c \cos\theta_{ca} + \cos^2\varphi_c \tag{7}$$

$$\cos \eta_{fa} = \sin^2\varphi_f \cos\theta_b - \cos^2\varphi_f \qquad (8)$$

$$\cos \eta_{fb} = \sin^2\varphi_f \cos\theta_{fa} + \cos^2\varphi_f \qquad (9)$$

$$\alpha = \frac{\eta_{cb} - \eta_{fb}}{2} \qquad (10)$$

In a partially folded state termed the "ring configuration," the doubly curved array inscribes an equivalent spherical segment geometry of radius R_0 spanning an angle from θ_1 to θ_2, as shown in Figure 2(c). The outer and inner profiles, number of unit cells, and the angular span of the array determine the similarity of the array to an ideal spherical segment.

To create a doubly curved array that partially folds into the intermediate ring configuration, design rules must be followed. Here, Figure 1(e) shows the projected vertices of the array in a ring folded configuration onto a cylindrical coordinate with origin O. The average radius R_o and the radial gap between the two profiles δ determine the radii of the concentric circular profiles. The inner circle radius is therefore $R_{in} = R_o - \delta/2$, while the outer circle radius is $R_{out} = R_o + \delta/2$. The angular span of the doubly curved array is therefore governed by the Cartesian height h_z and by the offset distance h_0 from the spherical center S to the unfolded array center O (Figure 1(e)).

As shown in schematic Figure 1(d), the F-type vertices constitute the outer profile, while the C-type vertices constitute the inner profile. In order for the folded array to be bound by the profiles, equations (11) and (12) must be met for each ith circumferential vertex and jth radial vertex

$$\text{Outer profile}: \tilde{z}^f_{i,2j-1} = h_0 + \sqrt{(R_o + \delta/2)^2 - (r^f_{i,2j-1})^2},$$
$$j = 1, \ldots, (n+1) \qquad (11)$$

$$\text{Inner profile}: \tilde{z}^c_{i,2j} = h_0 + \sqrt{(R_o - \delta/2)^2 - (r^f_{i,2j-1})^2},$$
$$j = 1, \ldots, \text{floor}\left(\frac{2n+1}{2}\right), \qquad (12)$$

where *floor* takes the largest integer less than or equal to its argument, and $\tilde{z}^c$ and $\tilde{z}^f$ are the z locations of the C-type and F-type vertices of the folded structure with an offset h_o along the z-axis.

The height of the kth layer as shown in Figure 1(e) is

$$h_k = a_{ck} \cos(\eta_{ca}/2), \quad k = 1, 2, \ldots, 2n+1 \qquad (13)$$

Considering the base of the array on the $z = 0$ plane, Figure 1(e), the total height of the array h_z is then

$$h_z = \tilde{z}^c_{i,2n} \qquad (14)$$

An array is designed by choosing radial and circumferential numbers of unit cells in the array (m, n), span and sizes of the profile $(h_o, h_z$ and $R_o)$, and thickness of the profile δ as input (Figure 1(e)). The value of α in closed ring configuration of the array is found by equating angular span to 2π radians, that is

$$2\alpha(m-1) = 2\pi \qquad (15)$$

For the purpose of this research, the array has to be flat foldable and developable. The requirements are satisfied by the inequalities in equations (16) and (17) (Song et al., 2017)

$$\varphi_c > \frac{\pi}{4} \qquad (16)$$

$$\varphi_c + \varphi_f > \frac{\pi}{2} \qquad (17)$$

It is shown by Song et al. (2017) that there is a peak value for α where both equations (16) and (17) are satisfied and the array is both flat foldable and developable. Equation (18) enables θ_b of the designed structure to correspond to that peak position of α

$$\cos\theta_b = \frac{\sin 2\varphi_f(1 + \cos^2\varphi_c) - \sin 2\varphi_c(1 + \cos^2\varphi_f)}{\sin 2\varphi_f \sin^2\varphi_c - \sin 2\varphi_c \sin^2\varphi_f}$$
$$(18)$$

Using α obtained from equation (15) and the prescribed design parameters $(m, n, h_o, h_z, R_o,$ and $\delta)$, the remaining parameters can be found in the ring configuration of the doubly curved array. To determine the detailed array geometry, $6n + 9$ unknowns $(\varphi_c, \varphi_f, a_{fi}, \alpha_o, a_{ci}, b_i, \theta_{ca}, \theta_{fa}, \eta_{ca}, \eta_{fa}, \eta_{cb},$ and η_{fb}, where $i = 1, \ldots, 2n)$ are determined. Hence, $6n + 9$ equations, that is, equations (1) to (12), (14), and (18), are solved using a nonlinear least square solver to obtain the unknown parameters.

Using the array parameters obtained, the coordinates of the ith circumferential and jth radial vertex of the array in ring folded configuration are written in the cylindrical coordinate system as follows.

For C-type vertices, one obtains the following relations

$$r^c_{i,j} = \frac{b_j \sin\left(\eta_{fb}/2\right)}{\sin\alpha}, \quad i = 1, \ldots, m+1; j = 1, \ldots, 2n+1 \qquad (19)$$

$$\theta^c_{i,j} = 2(i-1)\alpha, \quad i = 1, \ldots, m+1; j = 1, \ldots, 2n+1 \qquad (20)$$

$$z^c_{i,1} = 0, \quad i = 1, \ldots, m+1 \qquad (21)$$

$$z^c_{i,j} = \sum_{k=1}^{j-1} (-1)^{k-1} h_k - h_0, \quad i = 1, \ldots, m+1; j = 2, \ldots, 2n+1 \qquad (22)$$

For F-type vertices, one obtains the following relations

$$r_{i,j}^{f} = \frac{b_j \sin(\eta_{cb}/2)}{\sin \alpha}, \quad i = 1, \ldots, m; \ j = 1, \ldots, 2n + 1 \tag{23}$$

$$\theta_{i,j}^{f} = (2i - 1)\alpha, \quad i = 1, \ldots, m; \ j = 1, \ldots, 2n + 1 \tag{24}$$

$$z_{i,j}^{c} = z_{i,j}^{f}, \quad i = 1, \ldots, m; \ j = 1, \ldots, 2n + 1 \tag{25}$$

The vertices of the array are thus obtained using equations (19) to (25) to define the facet areas enclosed in each quadrilateral shape. These vertices and facet areas are subsequently used in the acoustic modeling.

2.2. Acoustic modeling of the doubly curved array

The geometric model of the doubly curved array creates a tessellated spherical segment when the array is folded into the closed ring configuration (Figure 2(a)). Considering each facet to be a baffled vibrating piston, Rayleigh's integral is employed to determine acoustic pressure radiated by the facets (Lynd and Harne, 2017). At a field point (x, y, z), the radiated acoustic pressure delivered from all of the baffled facets is $p(x, y, z, t)$, as shown in Figure 2(a) and (b). By Rayleigh's integral and linear superposition, this acoustic pressure is written as

$$p(x, y, z, t) = j \frac{\rho_o \omega u_o e^{j\omega t}}{2\pi} \sum_{i=1}^{M} \left(\int_{A_i} \frac{e^{-jkD_i}}{D_i} dA_i \right) \tag{26}$$

The density of the fluid medium is ρ_0; ω is the angular frequency of the time-harmonic oscillation of each facet; A_i is the area of the ith facet; u_0 is the amplitude of the uniform, normal velocity over A_i; $k = \omega/c_0$ is the acoustic wavenumber with the sound speed c_0; $D_i = \sqrt{(x - x_i)^2 + (y - y_i)^2 + (z - z_i)^2}$ is the distance from the field point to the center of the ith area where (x_i, y_i, z_i) are the coordinates of the facet center; and M is the number of facets.

The attention of this research is on wave focusing behavior, thus necessitating the near-field modeling approach developed by Ocheltree and Frizzel (1989). By the approach, each wave-radiating area is discretized into a large number of smaller wave radiating areas. With continued discretization, the dimensions of the sub-areas are sufficiently small such that the far-field approximation is an accurate representation of the sound field for the whole array. This approach (Ocheltree and Frizzel, 1989) thus permits the prediction of near-field sound propagation using simplified far-field expressions for the sub-area sound radiation

from the facets. Here, N is the number of smaller discretized areas per facet, and $A_{i,g}$ and $D_{i,g}$ are, respectively, the gth area and distance on the ith facet contributing to the field point

$$p(x, y, z, t) = j \frac{\rho_o \omega u_o e^{j\omega t}}{2\pi} \sum_{i=1}^{M} \sum_{g=1}^{N} \frac{e^{-jkD_{i,g}}}{D_{i,g}} A_{i,g} \tag{27}$$

It must be noted that the facets facing away from the spherical center S will not contribute significantly to the acoustic pressure. Hence, the facets facing S are considered as active for sound generation, that is, $A_{i,g}$ are the areas of these active facets.

The sound pressure level (SPL) is computed by

$$SPL = 20 \log_{10} \left(\frac{p_{rms}(x, y, z, t)}{p_{ref}} \right) \tag{28}$$

Where rms is the root mean square value of $p(x, y, z, t)$ and the reference pressure in air is $p_{ref} = 20 \, \mu Pa$ and in water is $p_{ref} = 1 \, \mu Pa$. These modeling approaches for shaped acoustic transducers are widely used and verified for their efficacy in model prediction (Ebbini and Cain, 1991; Jensen and Svendsen, 1992; Ross et al., 2005; Wan et al., 1996; Zou and Harne, 2017).

3. Experimental validation of spherical transducer wave focusing

To validate the analytical model predictions of wave focusing from the doubly curved acoustic array, an experimental proof-of-concept array is fabricated and evaluated. A schematic representation of the analytical realization and photograph of the experimental array are, respectively, shown in Figure 2(a) and (b). The wave focusing behavior of a spherical segment transducer is also computed and contrasted to provide first comparison among the tessellated approximations and the nominally ideal wave focusing surface (Figure 2(c)). The results of these comparisons are reported here.

3.1. Design and fabrication of experimental array and spherical segment comparison

Figure 2(c) provides a schematic representation of a spherical segment transducer to which a comparison is drawn with the doubly curved array as characterized analytically and experimentally. For the spherical transducer, the whole surface of the segment facing the spherical center is considered to be vibrating and emits acoustic waves. For the ideal geometry Figure 2(c), the radius is $R_o = 49.3 \, cm$, height is $h_z = 8.05 \, cm$, and the angular spans are $\theta_1 = 30°$ and $\theta_2 = 7°$, which coincide with the associated portion of a spherical segment encompassed by the doubly curved array. The relationship among these parameters is given by
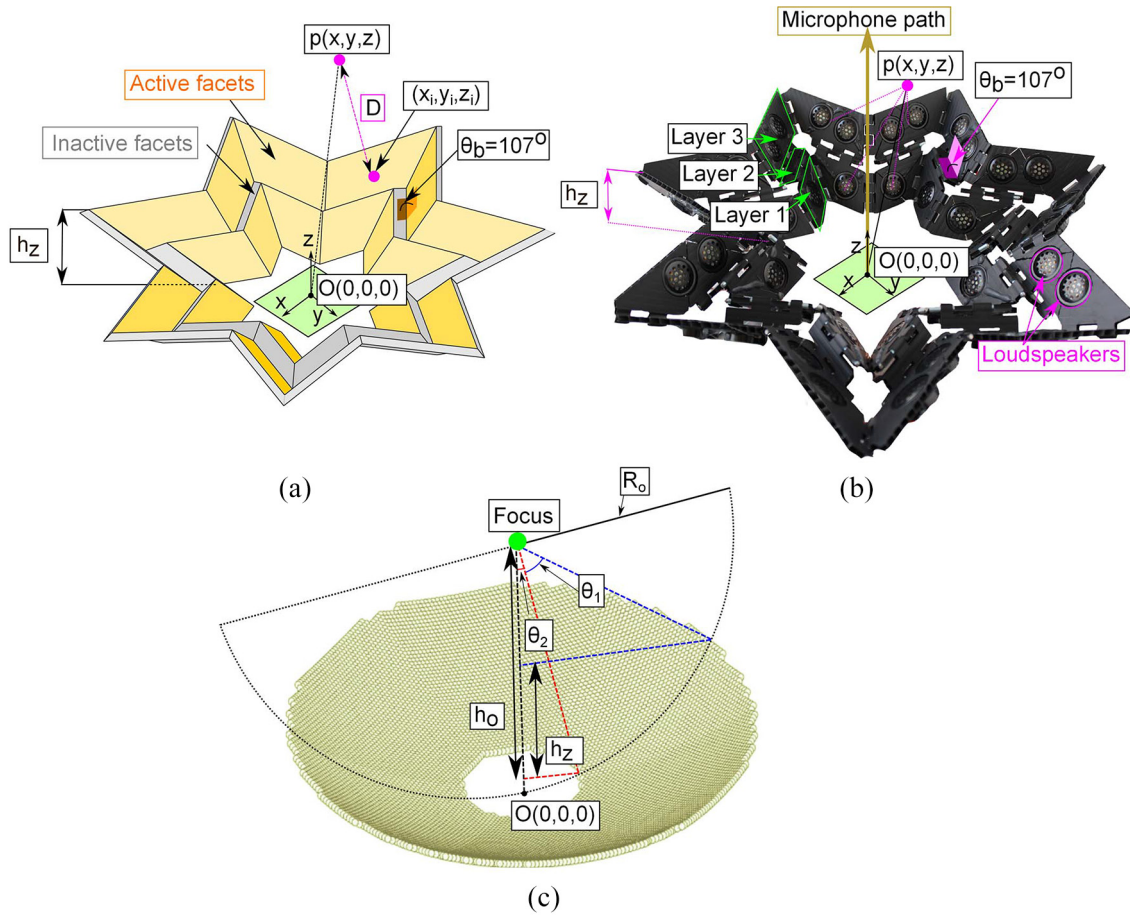
Figure 2. (a) Analytical model of 7 × 2 array, (b) proof-of-concept experimental array, and (c) model schematic representation of spherical segment transducer.

$$\cos \theta_1 = \frac{h_0 - h_z}{R_o} \qquad (29)$$

$$\cos \theta_2 = \frac{h_o}{R_o} \qquad (30)$$

The experimental array shown in Figure 2(b) is assembled from 7 × 2 unit cells. The array geometry is fully defined by $R_o = 49.30\,\text{cm}$, $\delta = 4.02\,\text{cm}$, $h_z = 8.05\,\text{cm}$, $h_0 = 49.80\,\text{cm}$, $m = 7$, and $n = 2$. Using the geometric model established in Section 2, it is found that the ring structure of the array occurs for a folding angle of $\theta_b = 107°$. Wave focusing behavior from the spherical segment transducer is characterized through a model employing techniques identical to those reported in Section 2.2.

The facets of the proof-of-concept experimental array are made from corrugated polypropylene sheet with 5 mm^2 corrugated cross sections. The thickness of the polypropylene layers making up the corrugated sheet is 0.3 mm. Each facet is broken into four separate areas so that the flutes of the corrugations are parallel with the edges of the facet (Zou and Harne, 2018). These sub-facets are cut using a laser cutter (Full

Spectrum Laser, Las Vegas, NV, USA) and re-assembled into the quadrilateral form with a miniature loudspeaker (Parts Express, Springboro, OH, USA) at the center. A loudspeaker is omitted in the reassembly process for the facets not facing the spherical center. The area of the facets in the second radial layer of unit cells is approximately twice the area of facets in the innermost layer of unit cells. As such, two mini-loudspeakers are employed in the outermost layer of unit cells for the facets facing the spherical center, as shown in Figure 2(b). Threaded rods are inserted through the fluted edges between adjacent facets to create a rotating hinge. Then, the structure is folded to $\theta_b = 107°$. To activate the facets uniformly as in the analytical model, the mini-loudspeakers are connected in serial and parallel combinations to deliver the same voltage amplitude to each loudspeaker.

3.2. Experimental setup

Measurements of the experimental array are taken inside a hemi-anechoic acoustic chamber of interior dimensions 7.78, 10.9, and 4.66 m. The acoustic array
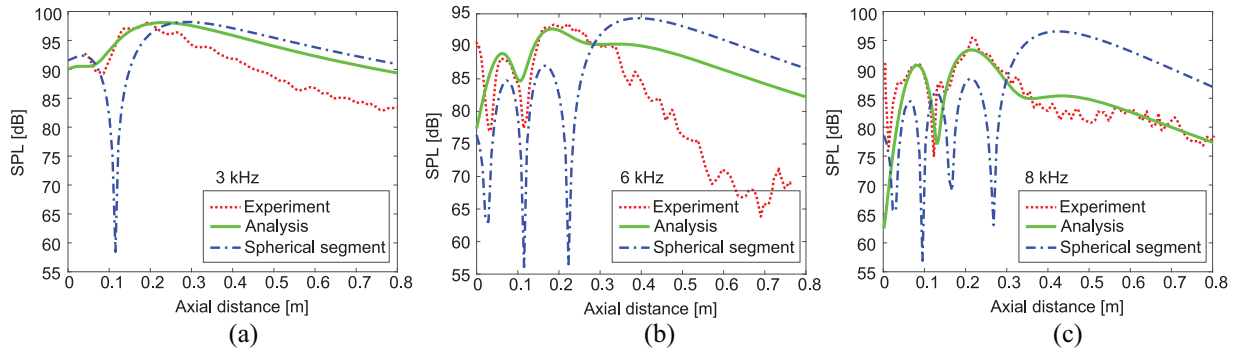
Figure 3. SPL along the axial distance, $z-$axis, for the experimental and analytical models of the doubly curved array, and for the spherical segment transducer. Frequencies of (a) 3 kHz, (b) 6 kHz, and (c) 8 kHz shown.

faces upward toward a ceiling of fiberglass wedges with a microphone traverse positioned to translate up and down along the directed axis of the array, as shown schematically in Figure 2(b). A draw wire displacement sensor is used to determine the position of the microphone (PCB 130E20). A single frequency signal sent to an audio amplifier (PFA330; Pyle, Brooklyn, NY, USA) projects to the array, while the microphone traverses along the $z-$axis, as identified in Figure 2(b). Data acquisition system (USB-6341; National Instruments, Austin, TX, USA) software is used to collect the pressure data recorded by the microphone. Pressure data are converted to SPL and processed in MATLAB using a fast Fourier transform to obtain a frequency spectrum at each axial point along the $z-$axis. The axial SPL at the driving frequency is subsequently determined from these results.

3.3. Comparison and discussion

To compare the experimental and analytical results, the normal velocity amplitude of the active facets in the analytical model is empirically determined to be $u_o = 630\,\mu\text{m/s}$. Figure 3 presents the SPL along the $z-$axis of the array for 3, 6, and 8 kHz obtained from the frequency spectrum.

The focal length is the distance from the array bottom center, such as the (x, y) plane in Figure 2(b), to the location of peak SPL along the central axis as shown in Figure 4. The focal lengths predicted analytically and measured experimentally for all frequencies 3, 6, and 8 kHz, as shown in Figure 3, uniformly agree. Likewise, here, we define the focal region as spatial extent of the greatest SPL highest peak, spanned by the spatial positions 3 dB less than the focal SPL. For 6 and 8 kHz in Figure 3(b) and (c), the focal regions agree quantitatively between experiment and analysis, whereas moderate discrepancy occurs for 3 kHz in Figure 3(a). For the analytical model, the full facet area is assumed to vibrate like a baffled piston, whereas in the experimental array, the mini-loudspeakers cover at

most around 75% of the facet surface. This distinction reduces the collective constructive interference phenomena that occur adjacent to the focal point and may thus provide one explanation for the discrepancies between analysis and experiment in terms of focal region and at axial distances more distant from the focus.

In comparison with the spherical segment transducer, the focal points found analytically and experimentally for the doubly curved array are closer to the array centers for all frequencies represented in Figure 3. Such a trend is explained by the tessellated composition of the doubly curved array, where the normals of the facets do not point to the spherical center described by the doubly curved geometry and instead converge to $z-$axis locations closer to the (x, y) plane. On the other hand, the SPLs at the focal points are in quantitative agreement for all cases shown in Figure 3, to within a few dB. Notably, the focal region of the spherical segment transducer is broader than for the analytical and experimental realizations of the doubly curved array. This indicates that the acoustic energy delivery for the ideal spherical segment is less focused than for the doubly curved array. These results both validate the analytical model for the doubly curved array and suggest that enhanced wave focusing may be realized by the tessellated array architecture due to the interference phenomena distinct to the faceted surface.

4. Investigations and discussions

Many applications of spherical transducers are for sake of focusing acoustic waves, for example, ultrasonic medical treatment (Kennedy, 2005), for which the acoustic impedance of the media is similar to water (Mast, 2000). In Section 4, the wave focusing abilities of the doubly curved acoustic array are studied in the ultrasonic regime, for a physically scaled array design considered to be operating in water. The assumption of linear acoustic wave propagation permits such direct physical scaling while retaining accuracy of model prediction. The scaling is performed by reducing the array

radius to 15 mm and giving attention to the frequency range around 500 kHz (Stephens et al., 2011), which exhibits qualitatively similar wave focusing behavior as the array in air around 5 kHz and with radius 49.3 cm. Here, the sound speed is 1500 m/s, density is 1000 kg/m^3, surface normal velocity amplitude is 66 nm/s, and reference pressure 10^{-6} Pa.

### 4.1. Focal similarity between doubly curved array and spherical segment transducer

Figure 4 presents the change of focal range as a function of frequency for doubly curved arrays having 16 × 4 unit cells and 41 × 7 unit cells, respectively. These range values are compared to the nominal radius of curvature forming the corresponding spherical segment.

Figure 4 reveals that the array with 16 × 4 unit cells exhibits a focal point closer to the array center (focal distance of 10 mm) at lower frequencies, with broad focal range shown by the corresponding dotted curves. Increase of frequency reduces the focal range but not to as great extent as for the array containing 41 × 7 unit cells. Figure 4 shows that the doubly curved array with 41 × 7 unit cells exhibits focusing precision throughout this ultrasonic frequency range via the small focal range with a focal point close to the spherical center. Such trend is intuitive on the basis of the greater proportion of a hemispherical shape encompassed in the array with 41 × 7 unit cells. At 960 kHz, both arrays shown in Figure 4 focus near the radius of curvature of the inscribed sphere, suggesting that the 960 kHz frequency is sufficient for contrasting array behaviors for broader ranges of design parameters. These parametric investigations follow in the next sections.

4.2. Focusing ability tailored by unit cell density and spherical shape approximation

The wave focusing characteristics of doubly curved arrays are then studied according to changes in array designs, governed by the number of radial unit cells, number of circumferential unit cells, distance δ between the circular profiles, and the height h_z of array. Throughout the studies in this Section 4.2, the radius of the array is 15.4 mm and the frequency of operation is 960 kHz in water.

In Figure 5(a), three doubly curved arrays with 4, 14, or 24 radial unit cells are compared to an ideal spherical segment transducer. The number of circumferential unit cells is 40. By increasing the number of radial unit cells, the normal from each facet points more closely to the spherical center. As seen through the results in Figure 5(a), the greater number of radial unit cells enhances the similarity of the doubly curved array wave focusing to the ideal spherical segment transducer. In Figure
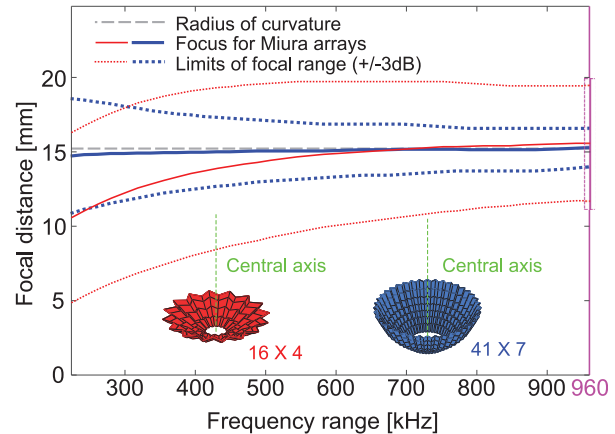

Figure 4. Focal regions obtained for arrays with 16 × 4 unit cells (red, thin curve) and 41 × 7 unit cells (blue, thick curve). Array 1: (h_0 = 15.56 mm, h_z = 3.14 mm, δ = 0.94 mm, R_o = 15.25 mm), Array 2: (h_0 = 15.56 mm, h_z = 12.58 mm, δ = 1.1 mm, R_o = 15.17 mm). Focal length is measured along the central axis from the array center.

5(b), the arrays employ five radial unit cells and 20, 30, or 40 circumferential unit cells. Such increase in the number of circumferential unit cells likewise suggests a convergent behavior to emulate the wave focusing of the ideal spherical segment transducer. On the basis of these observations, the results agree with intuition that increasing the number of facets better emulates the hemispherical nature of the doubly curved array, thus leading to more precise wave focusing.

In Figure 5(c), arrays with distinct distances δ between the circular profiles are compared for focusing characteristics. The distance δ is labeled in the central schematic representation of Figure 5. Here, $\delta = 0$ represents the ideal spherical segment because the inner and outer profiles are coincident. Intuitively it can be said that an array with the least distance δ most resembles the spherical segment, shown in Figure 5(c). Yet, the trend is not uniform since wave focusing for $\delta = 1.9$ mm is notably reduced. For the frequency of 960 kHz, the wavelength of waves in water is 1.56 mm, which is relatively close in value to the distance $\delta = 1.9$ mm between the curved profiles of the array. Such similarity results in destructive interference that evidently reduces wave focusing near the nominal focal point. Hence, to obtain wave focusing characteristics with the doubly curved acoustic array, the spacing between the profiles of the folded tessellation must be less than the wavelength so that the phase difference from adjacent facets to the common field point is minimal.

The influence of projected height h_z of the doubly curved array on the focusing behavior is examined in Figure 5(d). The projected height h_z is illustrated in the central schematic representation in Figure 5. By increasing the projected height of the array while the number of unit cells remains the same in radial and
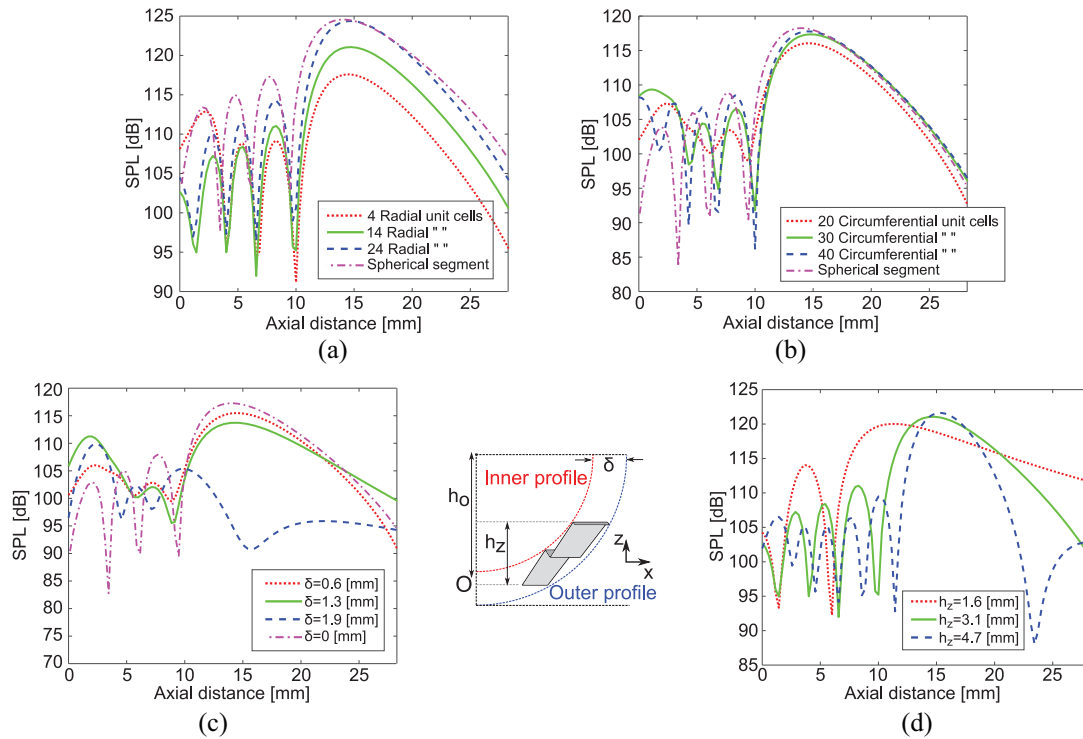
Figure 5. Parametric influences on wave focusing: (a) change of radial facets ($m = 40$, $h_0 = 15.25$ mm, $h_z = 4.7$ mm, $\delta = 0.63$ mm, $R_o = 15.4$ mm), (b) change of circumferential facets ($n = 5$, $h_0 = 15.25$ mm, $h_z = 3.14$ mm, $\delta = 0.63$ mm, $R_o = 15.4$ mm), (c) change of distance between curves ($m = 18$, $n = 5$, $h_0 = 15.25$ mm, $h_z = 3.14$ mm, $R_o = 14.77$ mm), and (d) change of height of the array ($m = 40$, $n = 14$, $h_0 = 15.25$ mm, $\delta = 0.63$ mm, $R_o = 15.4$ mm).

circumferential directions, the surface area inclined toward the spherical center increases. Intuitively, increase in surface area projecting toward the spherical center suggests increase in both focal intensity and SPL. Indeed, Figure 5(d) reveals that arrays with larger heights h_z lead to more intense wave focusing.

In general, the results of Section 4.2 reveal that doubly curved arrays, most emulating a spherical segment, lead to effective wave focusing. On the other hand, only certain combinations of m, n, h_o, h_z, δ, and R_o generate closed ring tessellations. Thus, geometric analysis is required to ensure dimensional feasibility before acoustic investigations may proceed.

4.3. Influence of projected surface area

The projected surface area of the doubly curved array that most emulates the spherical segment best focuses waves near the focal point. Here, Section 4.3 examines how many facets and how refined of a tessellation topology are required to achieve considerable elevation in the focal point SPL. The focal point SPL values for arrays of varied similarity to the spherical segment are compared as a function of projected surface area in Figure 6. To achieve this increase in projected surface area, the distance δ between curved profiles and the height h_z of the projected array must also vary to

enforce geometric compatibility. The parameters used in the modeling are shown in Figure 6.

The inset text in Figure 6 shows that the focal point shifts from 12.0 mm for an array with small projected area to 15.7 mm for an array substantially emulating a spherical segment transducer. This result agrees with findings in Figure 3. In addition, the SPL at the focal point increases with increase in the projected surface area, agreeing with intuition. On the other hand, by an order of magnitude increase in the projected surface area, the acoustic pressure amplitude change at the focal point is only 5.6 times, suggesting a disproportionate reduction in simplicity of design compared to the wave focusing benefit. In consequence, one may conclude that the use of fewer circumferential and radial unit cells is a more practical approach by which to realize effective wave focusing with a more straightforward array design to implement.

4.4. Comparison of full-field response in acoustic near field

The examinations in Sections 4.1, 4.2, and 4.3 show that wave interference near the focal point may be similar for doubly curved arrays and spherical segment transducer counterparts according to strategic selection of the array design parameters. Here, these similar
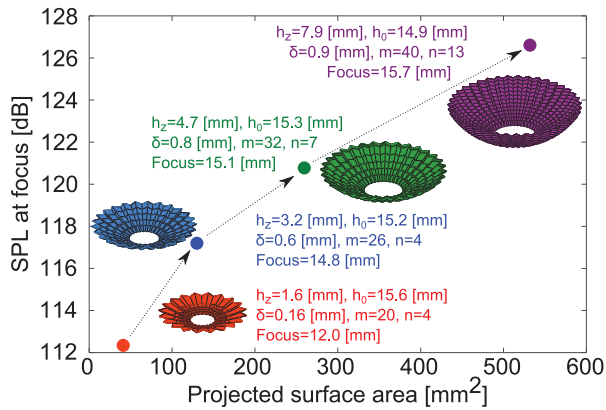
Figure 6. Increasing order of spherical nature from bottom to top, depicting increasing SPL and improved focus. The radius of each array is R_o = 15.625 mm.

transducers are compared based on wave field at and around the focal point to understand the detailed

interference phenomena involved. In Figure 7, each left half of the sub-figure shows the normalized acoustic pressure amplitude for the doubly curved array in the field, while the right half of the sub-figure presents the corresponding results for the spherical segment encompassing the same angular extent as the array. The white line between left and right halves of each sub-figure is for ease of visualizing the division between figure parts.

At 450 kHz, the array with 10×3 unit cells in Figure 7(a) provides substantially similar wave focusing, in terms of focal breadth and amplitude, as the counterpart spherical segment transducer. On the other hand, the near field close to the array surface shows local fluctuations of acoustic pressure distinct from those of the ideal segment. Yet, by increasing the frequency to 960 kHz in Figure 7(b), the wave interference from the 10×3 array is insufficient to emulate the wave focusing of the spherical segment as plainly observed by the drastic contrast between near field and
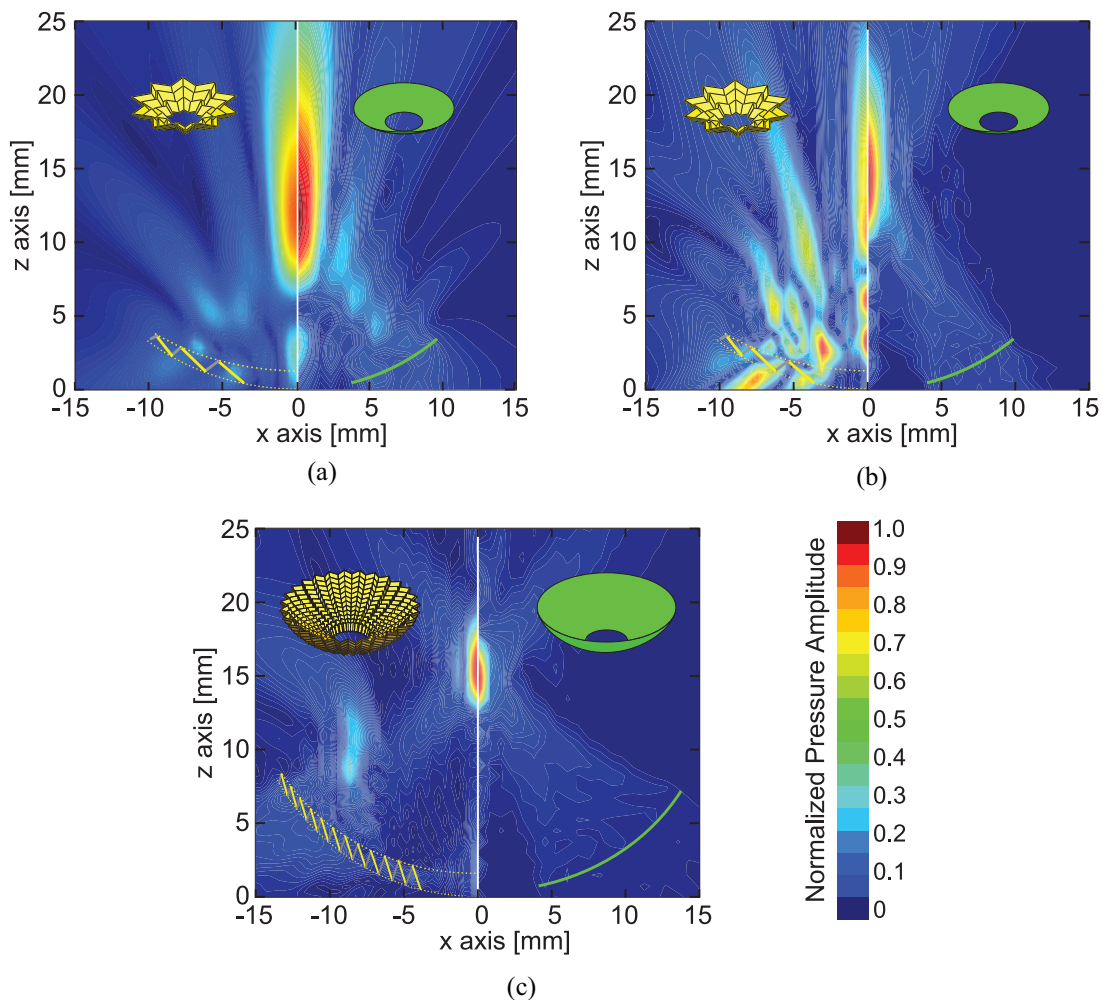
Figure 7. Near-field normalized acoustic pressure amplitude for 10×3 array (h_0 = 15.25 mm, h_z = 3.14 mm, δ = 1.58 mm, R_o = 14.93 mm) at left and for equivalent spherical segment at right at (a) 450 kHz and (b) 960 kHz. (c) Near-field normalized acoustic pressure amplitude for 28×12 array (h_0 = 15.25, h_z = 7.86 mm, δ = 1.58 mm, R_o = 14.93 mm) at left and for equivalent spherical segment at right at 960 kHz. In (a, b, c), the radius of arrays and transducers is 15.6 mm.

focal point wave amplitudes in Figure 7(b) between the two systems. Figure 7(c) considers an array with 28 × 12 unit cells also driven at 960 kHz. In this case, the array is able to successfully emulate the focal point and overall wave field of the counterpart spherical segment. These findings show that the concept of the doubly curved acoustic array is able to realize nominally ideal wave focusing but not in a broadband manner: strategic design and implementation are required to capitalize on the concept in a simple array architecture. Taking advantage of the model and acoustic analysis of this report, one may design an array with the least number of radial and circumferential unit cells that delivers close-to-ideal wave focusing in an array platform that permits flat folding for unique portability in applications having challenging accessibility constraints.

5. Conclusion

This research explores wave focusing capabilities of doubly curved acoustic arrays formed by reconfiguring the tessellated acoustic transducer into a closed ring form. Profiles of a doubly curved array are designed according to definition of concentric circles in order to resemble a spherical segment. In the closed ring configuration, the wave radiating facets direct sound toward axial focal points. Following model development and experimental validation, this research finds that, contrary to intuition, complete emulation of spherical segment geometries is not needed to realize substantial wave focusing behavior. The frequency at which such advantages are borne out is strongly dependent upon the doubly curved array design, indicating that frequency selection provides a substantial constraint on potential array geometries that permit most effective wave focusing. Overall, this research identifies strategies for designing doubly curved acoustic arrays that achieve focusing capabilities similar to a spherical segment transducer. The flat foldability and developability of this array opens up a new approach to tackle problems of manufacturing, transport, and deployment for such focusing transducers to be used in medical practice (Ji et al., 2008), imaging (Cantinotti et al., 2018; Vilkomerson et al., 1992), and so on. Furthermore, this research can be extended to study numerous curved profiles (Song et al., 2017) such as ellipses, parabolas, and more, which might have unexplored potential applications.

Declaration of conflicting interests

The author(s) declared no potential conflicts of interest with respect to the research, authorship, and/or publication of this article.

ORCID iD

Ryan L Harne 🅿 https://orcid.org/0000-0003-3124-9258

References

Alharbi S, Chaudhari S, Inshaar A, et al. (2018) E-textile origami dipole antennas with graded embroidery for adaptive RF performance. *IEEE Antennas and Wireless Propagation Letters* 17: 2218–2222.

Aronov B, Brown DA, Bachand CL, et al. (2012) Analysis of unidirectional broadband piezoelectric spherical shell transducers for underwater acoustics. *The Journal of the Acoustical Society of America* 131: 2079–2090.

Cantinotti M, Giordano R, Corana G, et al. (2018) Use of linear and convex ultrasound transducers for evaluation of retrosternal area in patients after cardiac surgery. *Echocardiography* 35: 100–103.

Cybulski JS, Clements J and Prakash M (2014) Foldscope: origami-based paper microscope. *PLoS ONE* 9: e98781.

Dudte LH, Vouga E, Tachi T, et al. (2016) Programming curvature using origami tessellations. *Nature Materials* 15: 583–588.

Ebbini ES and Cain CA (1991) A spherical-section ultrasound phased array applicator for deep localized hyperthermia. *IEEE Transactions on Biomedical Engineering* 38: 634–643.

Fernandes R and Gracias DH (2012) Self-folding polymeric containers for encapsulation and delivery of drugs. *Advanced Drug Delivery Reviews* 64: 1579–1589.

Gattas JM, Wu W and You Z (2013) Miura-base rigid origami: parameterizations of first-level derivative and piecewise geometries. *Journal of Mechanical Design* 135: 111011.

Jensen JA and Svendsen NB (1992) Calculation of pressure fields from arbitrarily shaped, apodized and excited ultrasound transducers. *IEEE Transactions on Ultrasonics, Ferroelectrics, and Frequency Control* 39: 262–267.

Ji YH, Li QL, Yang Y, et al. (2008) Newly progress and application of high intensity focused ultrasound in medical. *Chinese Journal of Medical Physics* 25: 759–780.

Kennedy JE (2005) High-intensity focused ultrasound in the treatment of solid tumours. *Nature Reviews Cancer* 5: 321–327.

Kinsler LE, Frey AR, Coppens AB, et al. (1999) *Fundamentals of Acoustics.* 4th ed. New York: Wiley-VCH.

Koduru JP and Rose JL (2012) Transducer arrays for omnidirectional guided wave mode control in plate like structures. *Smart Materials and Structures* 22: 015010.

Kuribayashi K, Tsuchiya K and You Z (2006) Self-deployable origami stent grafts as a biomedical application of Ni-rich TiNi shape memory alloy foil. *Materials Science and Engineering A* 419: 131–137.

Li Q, Tsai CS, Sottini S, et al. (1985) Light propagation and acousto-optic interaction in a LiNbO3 spherical waveguide. *Applied Physics Letters* 46: 707–709.

Liu X, Yao S, Cook BS, et al. (2015) An origami reconfigurable axial-mode bifilar helical antenna. *IEEE Transactions on Antennas and Propagation* 63: 5897–5903.

Lynd DT and Harne RL (2017) Strategies to predict radiated sound fields from foldable, Miura-ori-based transducers for acoustic beamfolding. *The Journal of the Acoustical Society of America* 141: 480–489.

Lynd DT, Zou C, Crump J, et al. (2017) Directive and focused acoustic wave radiation by tessellated transducers with folded curvatures. *Proceedings of Meetings on Acoustics* 30: 055010.

Mast TD (2000) Empirical relationships between acoustic parameters in human soft tissues. *Acoustics Research Letters Online* 1: 37–42.

Merkens KP and Oleson EM (2018) *Comparison of High-Frequency Echolocation Clicks (Likely Kogia) in Two Simultaneously Collected Passive Acoustic Data Sets Sampled at 200 kHz and 320 kHz* (National oceanic and atmospheric administration technical memorandum). Honolulu, HI: National Oceanic and Atmospheric Administration.

Myer JH and Cooke F (1969) Optigami: a tool for optical system design. *Applied Optics* 8: 260–260.

Ocheltree KB and Frizzel LA (1989) Sound field calculation for rectangular sources. *IEEE Transactions on Ultrasonics, Ferroelectrics, and Frequency Control* 36: 242–248.

Ross AB, Diederich CJ, Nau WH, et al. (2005) Curvilinear transurethral ultrasound applicator for selective prostate thermal therapy. *Medical Physics* 32: 1555–1565.

Song K, Zhou X, Zang S, et al. (2017) Design of rigid-foldable doubly curved origami tessellations based on trapezoidal crease patterns. *Proceedings of the Royal Society A: Mathematical, Physical and Engineering Sciences* 473: 20170016.

Stephens DN, Kruse DE, Qin S, et al. (2011) Design aspects of focal beams from high-intensity arrays. *IEEE Transactions on Ultrasonics, Ferroelectrics, and Frequency Control* 58: 1590–1602.

Tachi T (2009) Generalization of rigid-foldable quadrilateral mesh origami. *Journal of the International Association for Shell and Spatial Structures* 50: 173–179.

Ter Haar G (1999) Therapeutic ultrasound. *European Journal of Ultrasound* 9: 3–9.

Vilkomerson DHR, Gardineer B and Hojeibane H (1992) Quasi-omnidirectional transducers for ultrasonic electronic-beacon guidance of invasive devices. In: *Proceeding of the SPIE 1733, new developments in ultrasonic transducers and transducer systems*, San Diego, CA, US, 5 November 1992, pp. 154–165. International Society for Optics and Photonics.

Wan H, VanBaren P, Ebbini ES, et al. (1996) Ultrasound surgery: comparison of strategies using phased array systems. *IEEE Transactions on Ultrasonics, Ferroelectrics, and Frequency Control* 43: 1085–1098.

Williams EG (1999) *Fourier Acoustics: Sound Radiation and Nearfield Acoustical Holography*. London: Elsevier.

Wu X and Sherar M (2002) Theoretical evaluation of moderately focused spherical transducers and multi-focus acoustic lens/transducer systems for ultrasound thermal therapy. *Physics in Medicine & Biology* 47: 1603–1621.

Zirbel SA, Lang RJ, Thomson MW, et al. (2013) Accommodating thickness in origami-based deployable arrays. *Journal of Mechanical Design* 135: 111005.

Zou C and Harne RL (2017) Adaptive acoustic energy delivery to near and far fields using foldable, tessellated star transducers. *Smart Materials and Structures* 26: 055021.

Zou C and Harne RL (2018) Piecewise assembled acoustic arrays based on reconfigurable tessellated structures. *The Journal of the Acoustical Society of America* 144: 2324–2333.

Zou C, Lynd DT and Harne RL (2018) Acoustic wave guiding by reconfigurable tessellated arrays. *Physical Review Applied* 9: 014009.